Parametric Design, Aerodynamic Analysis and Parametric Optimization of a Solar UAV

Nuno António Silva
nuno.antonio.silva@ist.utl.pt

Instituto Superior Técnico, Lisboa, Portugal

May 2014

Abstract

The aim of this thesis was to develop and implement a computational process to enable the swift design of different UAV configurations and their aerodynamic analysis. To this end, a CAD tool using scripts was adopted to define the UAV external shape which was later imported into a CFD tool to generate suitable meshes. The test case consisted of a Long Endurance Electric UAV (LEEUAV), that was aerodynamically analyzed and parametrically optimized. While performing the aerodynamic analyses, turbulence models Spalart-Allmaras and $k - \omega$ SST, the later used in tandem with the $\gamma - Re_\theta$ transition model, were employed and their predictions compared with experimental data. Only the $k - \omega$ SST turbulence model and the $\gamma - Re_\theta$ transition model were employed in the detailed aerodynamic simulations. During cruise, the baseline LEEUAV presents a lift-to-drag ratio of 14.01, stall speed of 6.21 m/s and maximum cruise speed of 29.3 m/s. To enhance the baseline cruise performance, several parametric optimization and sensitivity studies were performed where its nose, wing and fuselage shapes were modified. With the nose shape modification proposal, the adverse pressure gradients that previously existed in that surface were reduced. With rounded wingtips, the wing long laminar separation bubbles were predicted to decrease. With the proposed wing root fairing, a region of separated flow that formed beginning at 2° disappeared thus reducing the aircraft drag. With the proposed wing washout, aileron control effectiveness was extended to angles of attack up to 10°.

Keywords: Solar UAV, UAV Airframe, Long Endurance, Computational Fluid Dynamics, Parametric Modeling, Sensitivity Analysis.

1. Introduction

This thesis aims to make use of the current computer capabilities of both commercial and open source software packages by developing a design tool that enables the swift design of complex Unmanned Aerial Vehicles (UAVs) geometries through the use of Computed-Aided Design (CAD) tools but also provides rapid and reliable aerodynamic data to validate specific UAV configurations given key mission objectives. This tool was developed with the objective of being in between the conceptual and detailed UAV design phases so that after designing a specific UAV configuration the engineer would send that model into a Computational Fluid Dynamics (CFD) software and collect specific aerodynamic data.

This thesis takes part in a project proposal by the name of Long Endurance Electric UAV (LEEUAV) whose goals are the development of a low cost, small footprint, easy to build and maintain multirole electric UAV, capable of being deployed from short airfields and highly flexible so that it is able to adapt to different civilian surveillance missions, thus not being restricted to specific mission profiles. Although such a project covers numerous areas of expertise, this thesis focuses on completing a cycle that begins with the definition of a UAV geometric parameters, building that UAV geometry using custom made scripts using a CAD program, sending that geometry to a CFD software where high-fidelity aerodynamic analyses are performed and, finally, collecting and analyzing that aerodynamic data.

In this thesis, the LEEUAV will be the object of the geometric modeling, aerodynamic analyses and parametric optimization.

2. Parametric Design

FreeCAD [1] was the selected CAD tool for the LEEUAV design. This program proved to be very efficient in the parametric modeling of common UAV geometries. This software is customizable and allows the parametric modeling of complex three-dimensional geometries. It is open source and most of its functions are accessible using Python scripts

and if not, the user can develop new ones. It can also read and write open file formats such as STEP, IGES and STL which can then be used by the CFD software.

The design scripts were developed in such a way that the geometric design of a general UAV configuration can be divided into five main parts: the loading of the FreeCAD different modules required to run its native functions and the definition of specifically developed functions, the statement of a UAV geometry parameters required for the complete definition of its airframe components, the test of those parameters to ensure their relative dimensions are valid, the building and assembly of the different components and the export of the generated mesh and object files later used by the CFD software. The design scripts divide the geometry in four different but dependent geometries, namely its wing, fuselage, tail and nose. After building each component, they are assembled into a single entity so that the subtraction between the UAV and the computational control volume used in the aerodynamic analyses is easily performed.

The LEEUAV building process starts with the left half wing, defined by four sections. At each section one airfoil is specified, together with five additional variables which are the airfoil chord, wing sweep, twist and dihedral angles, and each section spanwise location. The airfoil used in all sections, was especially developed for this project using an in-house gradient based shape optimization tool coupled to the aerodynamic analysis tool XFOIL [2]. After building and assembling the wing, the fuselage is built section by section, until the final geometry is fused together into a single entity. The fuselage was built using a total of ten different cross-sections placed along its longitudinal axis to guarantee a smooth geometric transition between them. The LEEUAV tail has a characteristic inverted cruciform shape. Much of the tail building process is identical to that of the wing. The tail has a total of five sections which are defined by the location of different airfoils and their angles. The real nose geometry is comprised of a spinner, propeller and electric motor. However, the flow going around such geometries would probably cause unsteady phenomena that would require the use of unsteady schemes in the aerodynamic simulations. To avoid that, a simple ellipsoid geometry was produced to emulate the nose geometry. The control volumes employed in the aerodynamic simulations and used to refine specific areas of the aircraft meshes were developed using the design script. A total of five parallelepipedic control volumes were defined: two control volumes that cover the entire wing, another control volume that englobes the aircraft geometry comprised between the nose and half the tail boom, a fourth control volume that englobes the entire aircraft and a fifth that serves as the aerodynamic simulation control volume.

After building every LEEUAV component and fusing them all together, these are exported in three different file formats: STEP, IGES and STL files. All file types are easily imported into the CFD software.

The LEEUAV dimensions and views are provided in Table 1 and Figure 1.

Table 1: LEEUAV dimensions. [3]

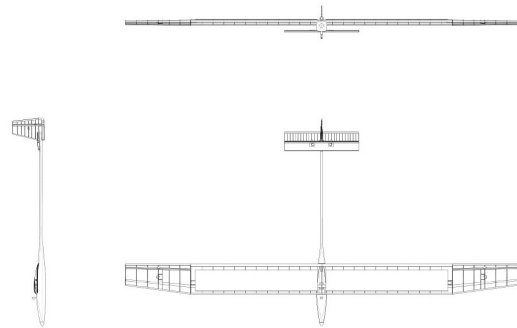|	
Wingspan	4.5 m
Length	2.37 m
Wing root chord	0.350 m
Wing tip chord	0.25 m
Wing planform area	1.5 m^2
Wing aspect ratio	13.5
Tailplan chord	0.213 m
Tailplan span	0.85 m
Tailplan planform area	0.181 m^2
Empennage root chord	0.258 m
Empennage tip chord	0.364 m
Empennage planform area	0.077 m^2

Figure 1: LEEUAV views. [3]

3. Turbulence and Transition Models Validation

When designing a specific airplane configuration, an engineer might use the classical theories of aerodynamics in a pre-design phase to get a grasp of the forces, moments and general flow physics the airplane will experience. However, in most cases, CFD simulations and possibly wind-tunnel tests for validating and experimenting with new configurations will be performed at a later stage. In the present work, CD-adapco's Star-CCM+ [4] was employed in all the in-depth aerodynamic analyses. This software does all the pre-processing, including mesh

generation, processing and post-processing. Besides Star-CCM+, XFOIL was also employed in cases where no wind-tunnel data was available.

Before performing the aerodynamic simulations on the entire LEEUAV, several mesh and aerodynamic model studies were carried out on simpler geometries. Because there was no wind-tunnel data for the LEEUAV airfoil, there was the need to find well studied airfoils subject to flows at Reynolds numbers similar to those of the LEEUAV during its cruise flight phase. Two airfoils, MA409 and CAL1215J, that fit this project objectives were selected. All data concerning these airfoils was obtained from the University of Illinois at Urbana-Champaign (UIUC) Aerodynamics Research Laboratory in its low-turbulence subsonic wind-tunnel [5]. Two turbulence and transition models were employed in the validation tests: the Spalart-Allmaras (SA) [6] turbulence model, that was sporadically employed with Turbulence Suppression model, and the $k-\omega$ SST turbulence model [7] that was always used with the $\gamma - Re_\theta$ [8] [9] transition model.

The LEEUAV was designed to fly at Reynolds numbers regimes of about 1.6×10^5 and Mach numbers of approximately 0.02, corresponding to air properties at 1,000 m above sea level ($\nu = 1.5810^{-5}$ m^{2}s^{-1}, a=336.4 m/s), airplane mean chord of 0.35 m and design cruise speed of 7.59 m/s.

Both airfoils were subjected to two Reynolds flow regimes and these were $Re_1 = 2 \times 10^5$ and $Re_2 = 3 \times 10^5$. A comparison between the airfoil simulations and experimental data proved that both turbulence models at either Reynolds number can accurately determine the lift coefficient. However, that is not the case when comparing the drag coefficient data. In the majority of the simulations, the SA turbulence model fails to provide acceptable results, or at least, ones as good as the $k-\omega$ SST turbulence model. The SA turbulence model drag predictions exhibit decreasing discrepancies as the angle of attack increases. A consequence of using this turbulence model without a transition model is that the flow is turbulent starting near the airfoils leading edge. When testing an airfoil using a wind-tunnel, as the angle of attack increases so does the velocity peak that also moves closer to the airfoil leading edge. As the velocity peak increases so does the adverse pressure gradient that follows and it is at that region that the flow under the right conditions becomes turbulent over the airfoil surface. This means that the turbulent drag contribution increases as the angle of attack increases since natural transition occurs closer to the airfoil's leading edge. This way, the increasing SA turbulence model drag prediction accuracy at higher angles of attack might just be the result of the model's turbulent kinetic energy generation in areas where there should

not be any generation at all coupled with the airfoil upper surface transition location gradually moving in the direction of the leading edge. No transition model is available in Star-CCM+ to use with the SA turbulence model. There is however the Turbulence Suppression. While using this model the obtained C_l and C_d values are much closer to the UIUC data. However, as good as it may be, it is hardly a transition model since it is up to the user to define where turbulence is to be suppressed.

In all simulations using the $k-\omega$ SST turbulence model together with the $\gamma - Re_\theta$ transition model, the laminar flow that first develops at the airfoils surfaces grows unstable until at a certain point it transitions into a turbulent boundary layer. At low Reynolds numbers, and when the free-stream turbulence intensity is low, the flow starts as laminar and after the velocity peak, when the adverse pressure gradient is strongest, the laminar boundary layer separates. If the conditions are adequate, the flow then experiences laminar-turbulent transition and the boundary layer re-attaches forming a laminar separation bubble (LSB).

4. LEEUAV Airfoil Aerodynamic Performance

Following the validation tests, a series of aerodynamic simulations using XFOIL and Star-CCM+ were performed on the LEEUAV airfoil at the design Reynolds numbers. In these studies, only the $k-\omega$ SST turbulence model used together with the $\gamma - Re_\theta$ transition model were employed. Using XFOIL, a comparison study of where natural transition is predicted to occur is established. Figure 2 compares the predicted natural transition locations.
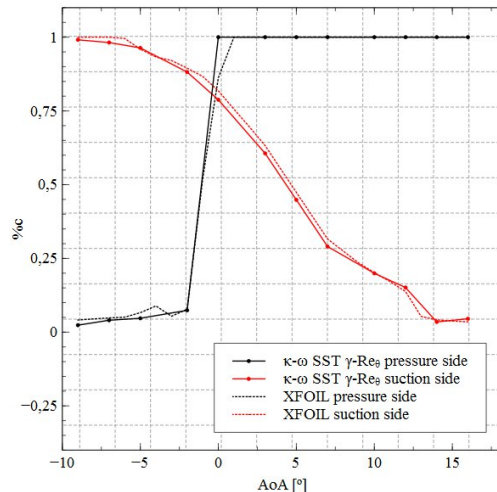

Figure 2: LEEUAV airfoil natural transition curves.

The mechanism in which transition occurs is the same as in the previous airfoil studies. Transition occurs gradually on the airfoil suction side. A lam-

inar separation bubble forms near the trailing edge and as the angle of attack increases that bubble decreases in length and moves closer to the leading edge. This gradual transition does not occur at the airfoil pressure side where no laminar separation bubbles are detected until angles of attack below 0° when the flow becomes turbulent at the leading edge.

Figure 3 shows the intermittency factor and regions of reversed flow at an angle of attack of 5°. Close to the surface, in the viscous sublayer, the intermittency factor equals zero. There is a region on the outer boundary layer where the intermittency is approximately 0.5 which is caused by the laminar separation which occurs upstream of the re-attachment point. This flow strip disappears in the downstream direction as the turbulent boundary layer thickness increases.
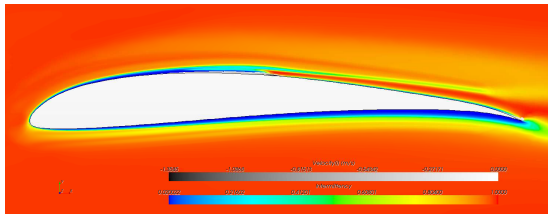
Figure 3: LEEUAV airfoil intermittency factor and regions of reversed flow, AoA=5°.

The LEEUAV has a solar powered assisted propulsion and as such its batteries may recharge as it flies by using the energy surplus generated by its solar panels. These solar panels are placed on top of its wing, which can be a source of problems by adding discontinuities to its surface which can produce effects similar to those of boundary layer trips. Two studies reproducing the effects of having offset surfaces on top of the LEEUAV airfoil were performed, simulating the effect of having solar panels on top of the wing. With the two-dimensional results one can infer what might happen at a three-dimensional level. These studies consisted of having two panel configurations: in configuration 1 a panel is placed on top of the original airfoil, thus increasing its thickness and adding two steps to the airfoil upper surface; in configuration 2 a tilted panel is added in order to have the panel trailing edge overlapping with the airfoil surface while maintaining the previous leading edge step. The solar panels used in these studies have a thickness of 2 mm and length of 256 mm.

Figure 4 shows the turbulent kinetic energy generation and regions of reversed flow around solar panel configuration 1 at an angle of attack of 5°. The simulations show that for both solar panel configurations the leading edge step promotes the formation of a laminar separation bubble in conse-
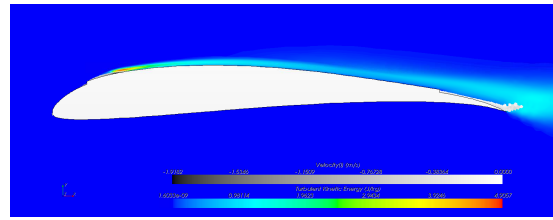

Figure 4: Solar panel configuration 1, turbulent kinetic energy (J/kg) and regions of reversed flow, AoA=5°.

quence of the sharp edge the flow encounters in its way, resulting in flow transition at that location. The flow behavior at the airfoils lower surfaces is the same as in the original airfoil shape. In configuration 1 the aft step promotes the formation and locking of a recirculation bubble.
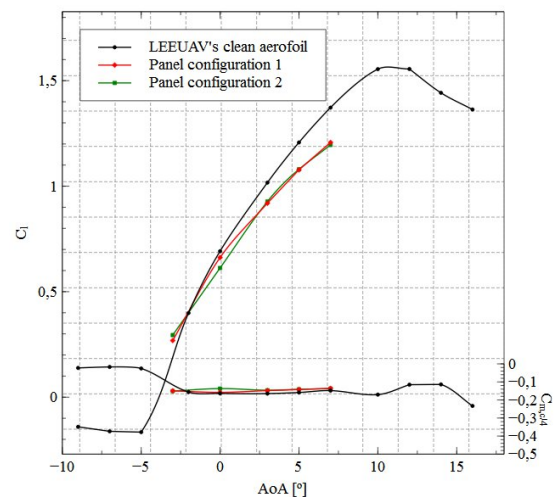

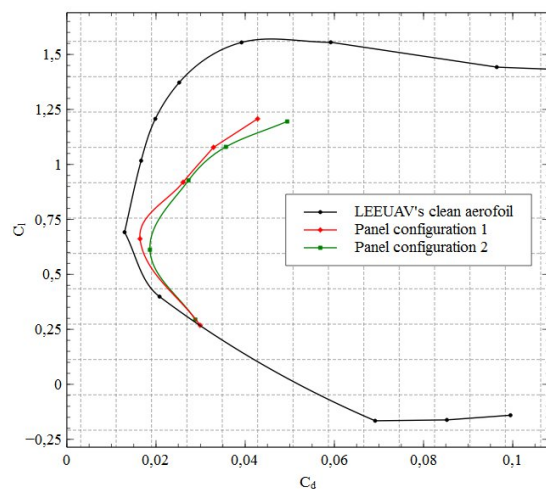Figure 5: LEEUAV airfoil, C_l and $C_{m,c/4}$ versus AoA.

Figure 6: LEEUAV airfoil, C_l versus C_d.

4

Both solar panel configurations promote the generation and fixation of a laminar separation bubble at their leading edge step. The implications are the forced transition at that location with the inherent drag penalties due to turbulence. Figures 5 and 6 show the comparison between the lift, quarter-chord point moment and drag coefficients of the clean airfoil and both solar panel configurations. For the tested configurations, placing a solar panel on top of the airfoil produces enormous penalties in both the lift and drag coefficients at any angle of attack. In terms of the moment coefficient, there is no significant difference between the three airfoil configurations. The solar panels that will eventually make part of the LEEUAV ought to be installed inside its wing, or if not, there is the need to implement a smooth surface transition between the airfoil and solar panels. The LEEUAV clean airfoil configuration shows good aerodynamic performance. This is a relatively thin airfoil and as such its C_l vs AoA curve is very characteristic. Looking at the extremes of the range of angles of attack in Figure 5, and recalling the airfoil transition curves, the high angle of attack lift loss is somewhat gradual in comparison with the lower angle of attack abrupt lift slope variation at -5°. The lift curve slope variation is rather abrupt at low angles of attack given the airfoil leading edge shape and the laminar separation bubble that develops there and later bursts. The aerodynamic performance data for the clean airfoil is listed in Table 2.

Table 2: LEEUAV airfoil aerodynamic performance table.

C_{lmax}	1.56
$\alpha_{C_{l max}}$	11°
α_{0lift}	-4°
$C_{l\alpha}$	6.15 rad^{-1}
C_{dmin}	0.0129
$C_{d,0}$	0.0207
$C_l/C_{d_{max}}$	61.03
$\alpha_{C_l/C_d max}$	3°
$C_l^{3/2}/C_{d_{max}}$	66.8
$\alpha_{C_l^{3/2}/C_d max}$	5°

5. LEEUAV Aerodynamic Performance

The physical models and settings employed in the full three-dimensional LEEUAV analyses are the same as those used in the two-dimensional analyses. A mesh with approximately 7 million cells was used in the three-dimensional aerodynamic simulations.

In the previous section it was understood that there are laminar separation bubbles present on the airfoil surfaces and, depending on the angle of attack, those bubbles change their location, length and thickness. The flow behavior and its intrinsic consequences found on the LEEUAV airfoil are present on its wing. The flow undergoes natural transition on the wing surfaces thus creating the well known laminar separation bubbles. Although at low angles of attack the bubbles thickness are relatively small, the wing effective shape does not remain the same which in turn affects the pressure field in its vicinity. Throughout the simulations, and depending on the angle of attack, there are long laminar separation bubbles located on the wing upper and lower surfaces. The wing lower surface LSB is only predicted to occur at negative angles of attack and can be quite extensive. Its presence is first detected at -4° and is located generally over the wing chord latter half. Its width is not the same throughout the wingspan. The bubble's width near the wing root is approximately 30%c, and gradually increases until it remains approximately constant and equal to 60%c near the wing tip. Its thickness is approximately one or two millimeters over the wingspan. As the angle of attack decreases to -6°, the bubble locates itself at the wing leading edge and its width is approximately half the wing chord. At this angle of attack the bubble width can be considered approximately constant over the entire wingspan and its thickness ranges from one to four millimeters. At -8°, the LSB width decreases even further and remains near the wing leading edge. At -10° the flow is no longer attached to the wing and there are large regions of separated flow.

The wing upper surface presents laminar separation bubbles at every simulated angle of attack and every bubble occupies approximately 90% of the wingspan. No laminar separation bubbles are detected on the wing area on top of the fuselage and close to the wingtip. Below -6° there is only one small LSB located at the wing trailing edge. At -6°, the LSB is uniformly distributed over the wing upper surface and its width is approximately 30%c and is located at the trailing edge. As the angle of attack increases the bubble moves closer to the leading edge which is consistent with the airfoil simulations. In the angle of attack range of -6° to 0° the bubble width decreases to values of approximately 15%c. Figure 7 shows the wing upper surface bubble at 0°. In the angle of attack range of 2° to 4° the bubble naturally keeps moving closer to the leading edge but its width now increases to values of approximately 45%c. From then on, as the angle of attack increases even further, the bubble width gradually decreases while remaining close to the leading edge. It is also in this angle of attack range, located at the wing root and starting at the wing leading edge, that a region of separated

flow starts to develop. As the angle of attack increases the flow region where the flow is separated grows even further. Figure 8 shows this region of separated flow at an angle of attack of 8°. After 8°, when the lift coefficient reaches its maximum value, the leading edge bubble bursts at several locations along the wingspan and consequently the flow is no longer attached to the wing surface which in turn produces massive lift loss. The regions where separated flow occurs start at the leading edge which, in terms of lift loss, present what is typically known as leading edge loss. Figure 9 evidences the regions of separated flow at 10°. That figure also shows that near the wing surface where the ailerons will be located the flow is also separated. This means that at high angles of attack, when the flow is separated in most of the wing surface, there is no way of controlling the LEEUAV roll actuating surfaces. Depending on the angle of attack, the wing upper surface bubble thickness presents different values. In general, away from the wing root region and while the bubbles have not burst yet, its thickness ranges between one and six millimeters.
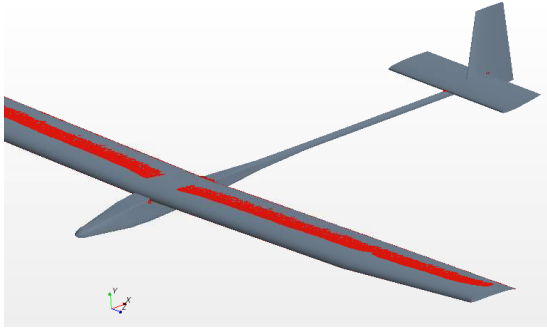

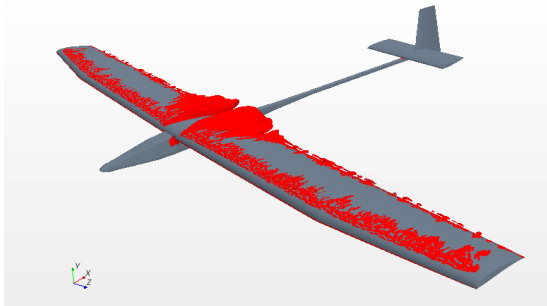Figure 7: Spanwise upper laminar separation bubble, AoA=0°.

Figure 8: Wing upper surface flow separation, AoA=8°.

Figure 10 gives an idea of the transition process at an angle of attack of 0° by showing in red the isosurface where reversed flow is detected and in blue the isosurface of the turbulent kinetic energy which gives an idea where the flow is expected to be tur-
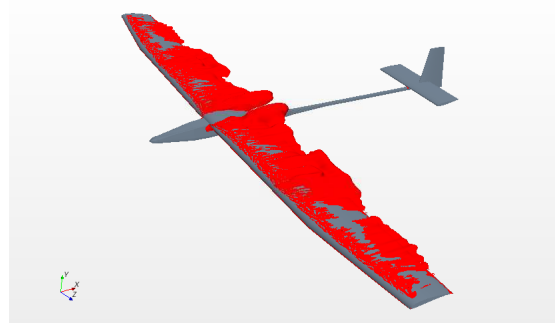
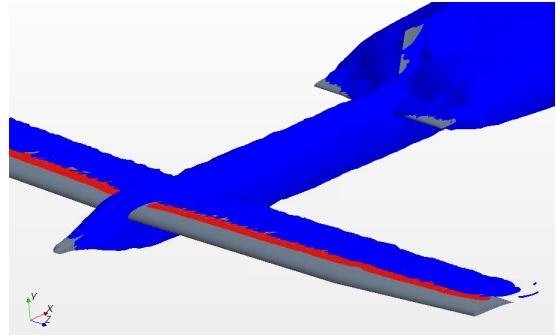

Figure 9: Wing upper surface flow separation, AoA=10°.

Figure 10: Isosurfaces of reversed flow (red) and turbulent kinetic energy (blue), AoA=0°.

bulent. The flow first becomes turbulent after going around the LEEUAV nose where it encounters adverse pressure gradients. Afterwards, the turbulent boundary layer grows and propagates over the fuselage, boom and tail. This figure shows that the horizontal and vertical stabilizers inner surfaces are in the turbulent wake region being shed from the fuselage. The transition model predicts bypass transition in these surfaces as a consequence of the high local freestream turbulence intensity from the wake. Outside the wake, the local freestream turbulence intensity is low and as a result the transition model predicts natural transition. These results are in line with the obtained results from reference [10]. As it would be expected, the flow becomes turbulent after the wing separation bubbles.

Figures 11 and 12 show two contour plots of the skin friction coefficient in the wing and tail surfaces. Figure 11 shows an increase in the skin friction coefficient after the laminar separation bubble and Figure 12 shows an increase in the skin friction coefficient on the inner tail surfaces. The skin friction increment verified on the wing is expected as a consequence of natural transition and the tail evidences bypass transition due to the fuselage turbulent wake. On the horizontal and vertical stabilizers, outside the turbulent wake, the skin friction coefficient gradually increases which leads to believe
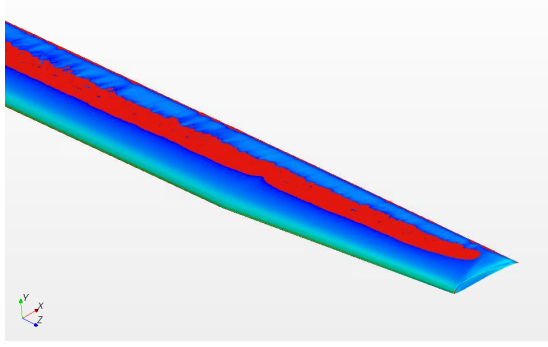
natural transition is predicted in those surfaces.

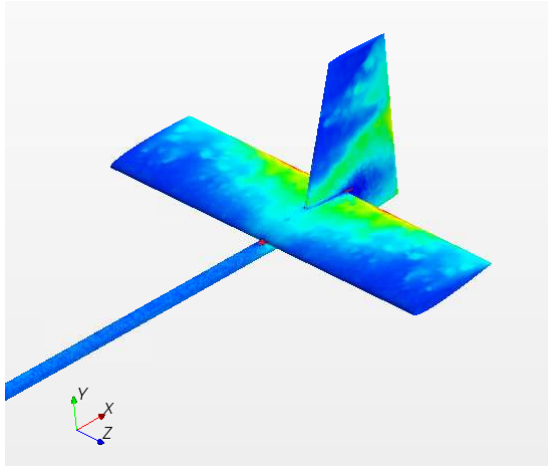Figure 11: Wing upper surface skin friction coefficient contour plot with reversed flow isosurface in red, AoA=0°.

Figure 12: Boom and tail surface skin friction coefficient contour plot with reversed flow isosurface in red, AoA=0°.
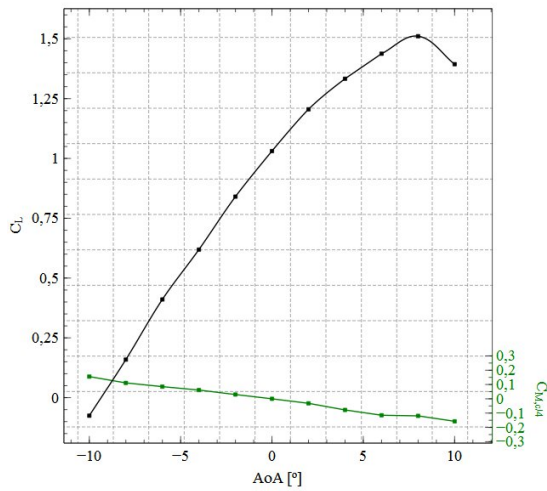

Figure 13: LEEUAV C_L and $C_{M,c/4}$ versus AoA.
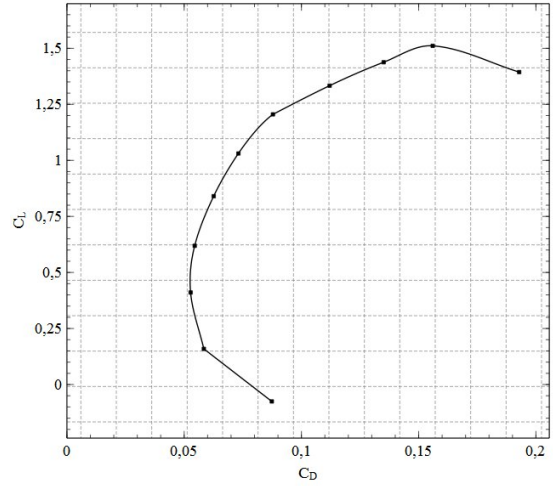

Figure 14: LEEUAV C_L versus C_D.

Figures 13 and 14 show the lift, quarter-chord moment and drag coefficients at the simulated angles of attack. A total of eleven angles of attack were simulated from -10° to 10°, with 2° increments. The moment coefficient, obtained at the quarter-chord point, evidences that the LEEUAV, as it was designed, is naturally stable. At positive angles of attack it produces a pitch-down moment whereas at negative angles of attack its tendency is the opposite. Table 3 summarizes the LEEUAV aerodynamic performance data. The LEEUAV cruise stall speed was determined to be 6.21 m/s, maximum cruise speed 29.3 m/s and maximum lift-to-drag ratio 14.01.

Table 3: LEEUAV aerodynamic performance table.

C_{Lmax}	1.51
$\alpha_{C_L max}$	8°
α_{0lift}	-9.5^o
$C_{L\alpha}$	5.59 rad^{-1}
C_{Dmin}	0.0527
$C_{D,0}$	0.06
$C_L/C_{D_{max}}$	14.01
$\alpha_{C_L/C_D max}$	0°
$C_L^{3/2}/C_{D_{max}}$	15.06
$\alpha_{C_L^{3/2}/C_D max}$	2°

As a matter of curiosity, the Spalart-Allmaras turbulence model was employed in the LEEUAV aerodynamic simulations an its results compared with the $k - \omega$ SST model predictions. In general, the lift data obtained with the SA model is in accordance with the $k - \omega$ SST model for angles of attack smaller than 6°. Although at high angles of attack the SA model lift predictions fail to detect

7

lift loss, at low angles of attack, its results are very similar to the ones obtained with the $k-\omega$ SST model. As for the drag coefficient, like it was the case when analyzing the airfoils, the SA turbulence model fails to produce aerodynamic data that is in line with what the $k-\omega$ SST model presents. Generally the percentile discrepancy between the two models is in the range of 15% to 25%. Although the SA model predictions fail to provide accurate lift data at high angles of attack and the computed drag data is underpredicted when compared to the $k-\omega$ SST model, it provided swift simulations requiring only 36% of the time.

6. Parametric Optimization Studies

In the course of studying the flow around the LEEUAV at the different angles of attack, it was understood that some geometric characteristics should be subject to parametric studies and further aerodynamic considerations. As such, a few shape redesigns were proposed.

6.1. Rounded Wing Tips

The wingtip geometry, as it was originally designed, is truncated rather than having a rounded surface. The purpose of designing a rounded wingtip was to create a smooth surface without discontinuities that enabled the easier flow passage from the wing pressure side to its suction side [11]. Comparing the two configurations, it is understood that the recirculation bubbles located at the wingtip truncated region are now non-existent. Furthermore, with the new geometry and at 0°, there is a reduction in the upper LSB of approximately three centimeters. With the rounded wingtip, the wingtip vortex effectively moves in the fuselage direction thus proving the beneficial effects in reducing the wing LSB. In terms of lift and drag coefficients there are no significant gains although the wing drag coefficient decreased very slightly.

6.2. Wing Root Fairing

The LEEUAV wing root region was not designed to present a particularly smooth transition between the wing and fuselage surfaces. Not having a smooth geometric transition between those surfaces proved to generate undesired aerodynamic effects. One of those was the development, beginning at 2°, of a region of separated flow on the wing upper surface. As the angle of attack increased so did that region of separated flow. The wing root region is critical due to the intersection of two bodies with their own pressure distribution fields and boundary layers. If no geometric transition is employed, the drag build-up could, in the right conditions, dramatically increase in those areas. With the proposed wing root fairing, apart from the wing upper surface laminar separation bubble, the regions of reversed flow are now considerably smaller and their thickness is comparable to that of the LSB, if not smaller. Figure 15 shows the regions of reversed flow at 4° for the proposed wing root fairing design. With the proposed design, the lift coefficient is smaller although very similar to that of the original configuration. Due to the mitigation of the region of reversed flow in the wing root region, there is a decrease in the drag coefficient.
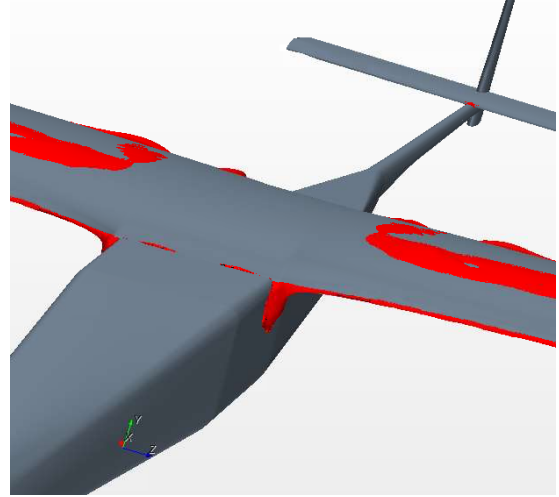

Figure 15: LEEUAV with wing root fairing and iso-surfaces of reversed flow in the wing root region, AoA=4°.

6.3. Nose Shape

The original nose design does not promote a smooth geometric transition with the fuselage. The original geometry, with its small length and angular generatrix produces significant adverse pressure gradients that promote flow transition. A solution to the original design was achieved by increasing the nose length by twenty millimeters and decreasing its generatrix curvature so that the geometric transition between the nose and fuselage became smoother. Figure 16 shows the nose pressure coefficient as a function of position, at an angle of attack of 0°. The proposed nose design evidences lower pressure gradients and pressure peaks. The proposed design almost does not present adverse pressure gradients at the simulated angle of attack, thus proving to be an improvement to the original design.

6.4. Wing Washout

Wing washout consists in reducing the lift distribution on the wing surface in the wingspan direction. There are a number of ways to adjust the lift distribution over the wing and one of those is ensured by reducing the wing section incidence angle from the wing root to the wingtip. The consequence is that, at high angles of attack, the flow that is expected to be detached in the wing root region is not at
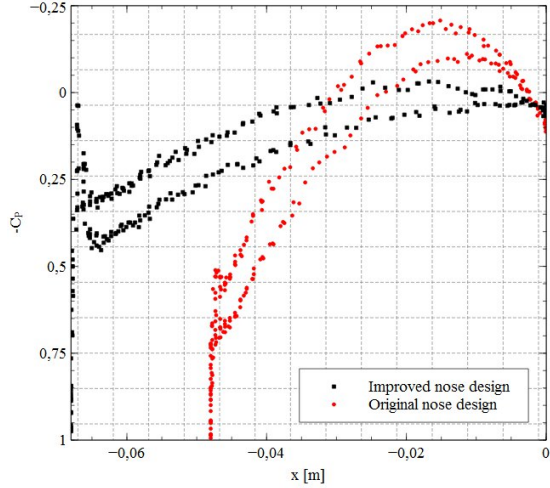
Figure 16: LEEUAV nose Cp curves comparison, AoA=0°.

the wing tip region. This way, controlling the aircraft trough the ailerons is still possible. In the new wing design proposal, the incidence angle nearing the wingtip is gradually reduced in 4°. Comparing Figures 9 and 17, at an angle of attack of 10°, the effects of the wing washout proved to be very positive with the wing region where the ailerons are located not evidencing boundary layer detachment. There was an expected decrease in the lift and drag coefficients.
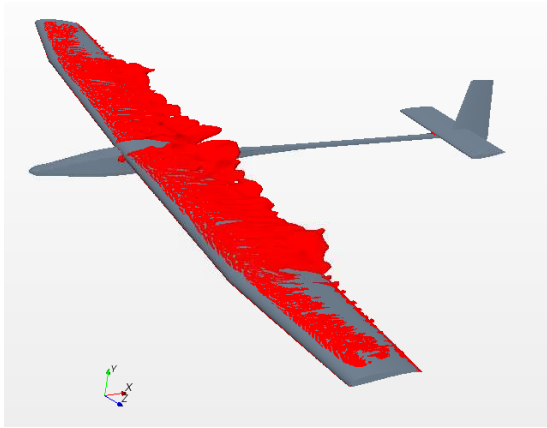

Figure 17: LEEUAV with wing washout isosurfaces of reversed flow, AoA=10.

7. Conclusions

The objectives of this thesis consisted in the development of a CAD tool that enabled the swift parametric design of generic UAV geometries and their aerodynamic evaluation using high-fidelity models. Furthermore, one UAV in particular, the LEEUAV, would be built using the developed CAD tool and aerodynamically evaluated and parametrically optimized.

Using FreeCAD as the CAD software package and the developed scripts, it was possible to not only design generic UAV geometries, but also to design a particular aircraft configuration, the LEEUAV.

Considering the aerodynamic simulations, prior to using specific physics, meshing and turbulence models, first there was the need to perform validation tests using reliable sources. During the validation phase two turbulence models were employed in the aerodynamic simulations where it was determined that only turbulence model $k - \omega$ SST used together with transition model $\gamma - Re_\theta$ provided valuable lift and drag data. During the LEEUAV airfoil aerodynamic simulations, two solar panel configurations were simulated in order to understand their effects when installed on the wing upper surface. From the performed simulations it was understood that both configurations forced flow transition at the panel's leading edge which in turn contributed to lift reduction and drag increase. The conclusion was that any solar panel installed on the wing must be allocated in such a way that no surface discontinuities are present. At a three-dimensional level, several aerodynamic simulations were performed having in consideration the LEEUAV cruise flight phase. The selected mesh and physics models allowed to capture aerodynamic phenomena such as the spanwise laminar separation bubbles along the wing, regions of separated flow beginning at the wing leading edge, the effects of the interaction between the fuselage and wing boundary layers and the flow bypass transition on the tail surfaces.

Turbulence model SA was also employed in the two- and three-dimensional aerodynamic analyses and the conclusions are that the lift coefficient is accurately predicted as long as the angles of attack do not increase to the point where flow separation is present in a significant way. The drag predictions differ between the two turbulence models because no transition prediction model was employed with the SA turbulence model. In terms of the required CPU time for the residuals to converge, the SA model is clearly superior. In conclusion, at low angles of attack and when one can manage to over- or under-predict an aircraft drag coefficient and when time is of the essence, the use of turbulence model SA is recommended. However, if there is the need to better predict the drag coefficient and associated phenomena, then turbulence model $k - \omega$ SST used with transition model $\gamma - Re_\theta$ should be employed.

Some geometric improvements were proposed to the baseline LEEUAV shape which consisted in modification of the wing, fuselage and nose geometries. All design proposals proved to enhance the LEEUAV flight performance at some level and further studies regarding their adaptation are recommended.

In terms of future work, there are a few concepts that might be interesting to think about. Only the cruise flight phase was considered in the LEEUAV design and three-dimensional analyses. However, during the entire flight profile a number of other flight conditions are encountered. It would be interesting to simulate the effects of crosswinds which are a common occurrence during takeoffs and landings, to simulate the effects of coordinated turns or to simulate the effects of control surfaces like the ailerons, rudder and elevators. Since the LEEUAV will require a landing gear it is also recommended to perform studies regarding its impact in the global aerodynamic performance. The LEEUAV will have a propeller in the nose region and its effects on the flow were not addressed. It would be interesting to do so since the propeller is transmitting energy to the fluid which should delay natural transition in the fuselage region.

Acknowledgements

References

[1] FreeCAD. https://www.freecadweb.org/, 2014.

[2] XFOIL. https://www.web.mit.edu/drela/public/web/xfoil/.

[3] A. C. Marta and P. Gâmboa. *Conceptual and Preliminary Design Summary Long Endurance Electric UAV*. 2013.

[4] CD adapco STAR-CCM+. https://www.cd-adapco.com/products/star-ccm/, 2014.

[5] Gregory A. Williamson, Bryan D. McGranahan, Benjamin A. Broughton, Robert W. Deters, John B. Brandt, and Michael S. Selig. *Summary of Low-Speed Airfoil Data*, volume 5. 2012.

[6] P. R. Spalart and S. R. Allmaras. A One-Equation Turbulence Model for Aerodynamic Flows. *AIAA*, 1992.

[7] F. R. Menter. Two-Equation Eddy-Viscosity Turbulence Models for Engineering Applications. *AIAA Journal*, Volume 32(Number 8), August 1994.

[8] F.R. Menter, R. B. Langtry, S. R. Likki, Y. B. Suzen, P. G. Huang, and S. Vlker. A Correlation-Based Transition Model Using Local Variables - Part I: Model Formulation. *Journal of Turbumachinery*, 128, July 2006.

[9] R. B. Langtry, F.R. Menter, S. R. Likki, Y. B. Suzen, P. G. Huang, and S. Völker. A Correlation-Based Transition Model Using Local Variables - Part II: Test Cases and Industrial Applications. *Journal of Turbumachinery*, 128, July 2006.

[10] R. B. Langtry and F. R. Menter. Transition Modeling for General CFD Applications in Aeronautics. *AIAA*, 2005.

[11] Sighard F. Hoerner and Henry V. Borst. *Fluid-Dynamic Lift Practical Information on Aerodynamic and Hydrodynamic Lift*. Mrs. Liselotte A. Hoerner, 1985.